Infrared probe of the bulk insulating response in Bi_{2−x}Sb_{x}Te_{3−y}Se_{y} topological insulator alloys

K. W. Post, Y. S. Lee, B. C. Chapler, A. A. Schafgans, Mario Novak, A. A. Taskin, Kouji Segawa, M. D. Goldflam, H. T. Stinson, Yoichi Ando, and D. N. Basov

Phys. Rev. B **91**, 165202 — Published 16 April 2015

DOI: 10.1103/PhysRevB.91.165202

An infrared probe of the bulk insulating response in $Bi_{2-x}Sb_xTe_{3-y}Se_y$ topological insulator alloys

K. W. Post,[1,*] Y.S. Lee,[1,2] B.C. Chapler,[1] A.A. Schafgans,[1] Mario Novak,[3] A.A. Taskin,[3] Kouji Segawa,[3] M.D.Goldflam,[1], H.T. Stinson,[1] Yoichi Ando,[3] and D. N. Basov[1]

[1]*Physics Department, University of California-San Diego, La Jolla, California 92093, USA*

[2]*Department of Physics, Soongsil University, Seoul 156-743, Republic of Korea*

[3]*Institute of Scientific and Industrial Research, Osaka University, Osaka 567-0047, Japan*

(Dated: March 13, 2015)

We have investigated the electronic structure and carrier dynamics of the topological insulator $Bi_{2-x}Sb_xTe_{3-y}Se_y$, for x=0.5, y=1.3 and x=1, y=2, using infrared spectroscopy. Our results show that both of these BSTS alloys are highly insulating in the bulk, with analysis of the infrared data indicating an upper limit to the carrier density of 4.4x10^{17} cm^{-3}. Furthermore, analysis of the interband transitions of $Bi_{1.5}Sb_{0.5}Te_{1.7}Se_{1.3}$ revealed distinct band structure critical points, which suggest high crystallographic order of our crystals. Motivated by the low carrier density and crystallographic order identified in these compounds, we searched for the Landau level transitions associated with the surface states through magneto-optical measurements in the far infrared range. We failed to observe any indications of the Landau level resonances at fields up to 8 T in sharp contrast with our earlier finding for a related $Bi_{1-x}Sb_x$ alloy [1]. We discuss factors that may be responsible for suppressed magneto-optics response of these single crystals.

The initial theoretical predictions [2–7] and subsequent experimental realization [8–13] of Dirac-like surface states (SSs) in topological insulators (TIs) has rapidly brought this new class of materials to the forefront of condensed matter physics [14–17]. The SSs in TIs are unique in that they host electrons that are resistant to direct backscattering and localization [2, 4, 5]. Moreover, SSs possess unique magnetoelectric properties that are predicted to yield a number of exotic effects, including an induced magnetic monopole, and quantized Kerr rotation [18–23]. It has also been proposed that these numerous exotic properties of SSs could be utilized in a plethora of technologies including quantum computing, spintronics, and improving current computer technology [15].

The key to studying the exotic intrinsic properties of TIs, is isolating the SS charge carriers from the bulk response, thereby achieving SS dominated conductivity. However, SS dominated conductivity has remained elusive, being observed only in a few cases [24–26] despite the large body of work focused on this issue. More commonly, vacancies and anti-site defects push the chemical potential (μ_F) into the bulk bands [27] so that the relatively weak SS conduction is masked by bulk dopants. One method for overcoming this issue is to combine n-type TIs (Bi_2Se_3 and Bi_2Te_3) with the p-type TI Sb_2Te_3 in alloys of form $Bi_{2-x}Sb_xTe_{3-y}Se_y$ [28–30], such that the p and n type defects compensate each other, resulting in a bulk insulating TI. A systematic transport study of $Bi_{2-x}Sb_xTe_{3-y}Se_y$ alloys has found high low temperature resistivity values in $BiSbTeSe_2$ (BSTS1) and $Bi_{1.5}Sb_{0.5}Te_{1.7}Se_{1.3}$ (BSTS2) of 5.5 and 4.5 Ω cm, respectively. These findings imply that bulk carriers are largely eliminated, and are highly promising materials for studies of SSs and potential applications [28] Furthermore, photoemission measurements of identically grown BSTS1 and BSTS2 alloys have revealed that μ_F is located within the bulk energy gap, at or near the SS Dirac point, indicating that these materials are ideal for surface dominated conductance.

Here we report infrared (IR) spectroscopy measurements on bulk BSTS1 and BSTS2 crystals grown as described in Ref. [28]. We initially characterized the bulk electronic properties of these samples using IR techniques, in the absence of an externally applied magnetic field. Analysis of the optical constants extracted from these measurements, detailed later in the text, reveals that both BSTS1 and BSTS2 are strongly insulating with effectively no signature of free carriers or impurity bands in the optical conductivity. Additionally, the analysis reveals that BSTS2 has both an exceptionally large energy gap of 0.35 eV, and shows characteristics IR features attributable to distinct critical points in the band structure. These band structure critical points (BSCP) are indicative of a high degree of crystallographic order, which is unusual for an alloyed system. Furthermore, we have used our optical conductivity spectra to establish upper limits on the bulk carrier density (n), revealing that the maximum value of n for both alloys is relatively small, being at most 4.5 x 10^{17} cm^{-3}. To directly study the SS properties, we performed infrared reflectivity measurements in high magnetic fields, a technique which has been used to characterized SSs in other TI materials [1]. In spite of the promising findings of the initial zero field infrared measurements, we did not observe the characteristic LL dispersion of SSs in these BSTS compounds.

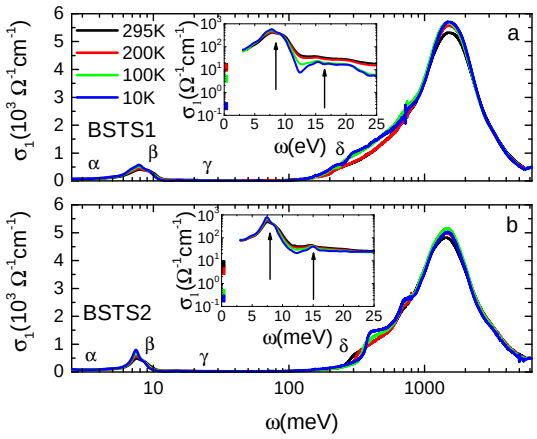

FIG. 1. The values of $\sigma_1(\omega)$ extracted from the IR spectra are shown for BSTS1 (a) and BSTS2 (b). The salient features of the spectra are the low ω region (α), the phonon peak (β), the intergap region (γ) and the onset of interband conductivity (δ). The α and β regions are detailed in the insets of (a) and (b), with the phonon center frequencies indicated by the arrows. The measured DC conductivities of identically grown samples are indicated by the squares along the y-axis, colored to match the corresponding temperature.

These data and possible reasons for this null result are discussed later in the text.

We obtained the zero-field IR spectra of BSTS samples using a combination of normal incidence reflectance and variable angle spectroscopic ellipsometry (VASE), which is discussed in more detail in the appendix. The sample optical constants were extracted by performing a Kramers-Kr onig (KK) inversion of the combined reflectance (R(ω)) and VASE datasets. The real part of the complex conductivity ($\sigma_1(\omega)$) was extracted from the KK fitting of the infrared data at all measured temperatures and the resulting spectra are shown in Fig. 1. These $\sigma_1(\omega)$ spectra can be divided into four regions of interest, with the corresponding label indicated in parenthesis: the low ω region (α), the phonon peak (β), the intragap region (γ) and the interband absorption region (δ), as indicated in Fig 1. The α region is related to the free charge carrier dynamics, and in the case of a simple Drude metal is described by the formula [31]:

$$\sigma_1(\omega) = \frac{ne^2\tau}{m^*}\frac{1}{1+(\omega\tau)^2} \qquad (1)$$

where m^* is the effective mass and τ is the scattering rate. However, the α region of our $\sigma_1(\omega)$ spectra show no indication of a Drude lineshape; rather the optical conductivity at low ω is small and decreases towards the measured DC value of conductivity, indicative of a band insulator. In the higher energy β region, there are two peaks in $\sigma_1(\omega)$ corresponding to the IR active phonons that have been observed previously in other similarly structured TI materials [32, 33]. These two phonons, indicated by the arrows in the insets to Fig. 1a and 1b, are centered at 62 cm^{-1} and 120 cm^{-1} (63 cm^{-1} and 117 cm^{-1}) for BSTS1 (BSTS2), and sharpen with cooling. An inspection of the phonon lineshapes reveals that the peaks are broader in BSTS1 than in BSTS2, implying lower disorder in the latter alloy. The conductivity in the interband region, γ, is small and featureless for both materials, as is typical of semiconductors. Importantly, we observed no indication of the impurity band which was observed in the related compound Bi_2Te_2Se [34, 35], and in identically grown $Bi_{2-x}Sb_xTe_{3-y}Se_y$ alloys [24].

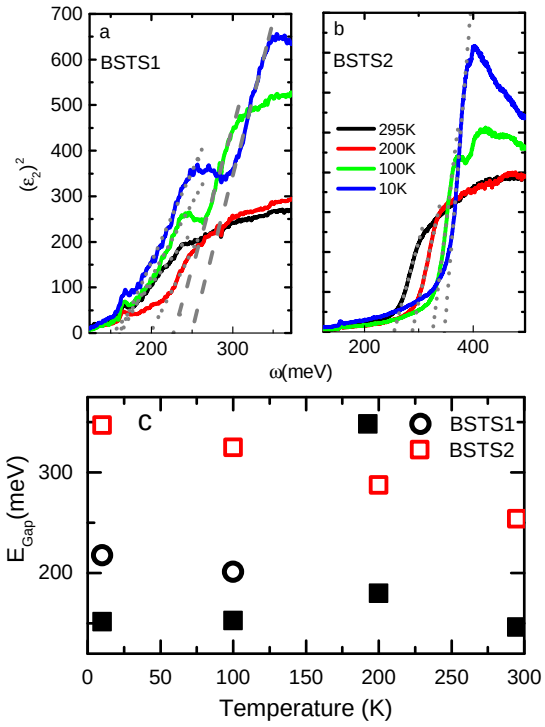

FIG. 2. The $(\epsilon_2)^2$ spectra of BSTS1 and BSTS2 are shown in (a) and (b), respectively. The linear region of $(\epsilon_2)^2$ indicates the direct band gap, and the x-axis intercept of the linear fits, indicated by the dotted gray lines, gives a numerical value for E_{Gap}. The values of E_{Gap} extracted using this method are plotted as a function of temperature in (c). With cooling, a second linear region emerges in BSTS1, which was fit at 100K and 10K as indicated by the dashed gray lines. The energy corresponding to this second interband transition is plotted in (c) as the black open circles.

The onset of interband transitions, which occur in the higher energy region δ, are indicated by the increase in $\sigma_1(\omega)$ near 2000 cm^{-1} for both BSTS1 and BSTS2. The energy gap (E_{Gap}) of these systems is precisely determined by the x-axis intercept of a linear fit to $(\epsilon_2(\omega))^2$

as prescribed in [36], where $\omega[s^{-1}] \cdot \epsilon_2(\omega[s^{-1}])/4\pi = \sigma_1(\omega)[s^{-1}]$ [31]. We show the $(\epsilon_2(\omega))^2$spectra for both BSTS1 and BSTS2 in Fig. 2a and Fig. 2b, respectively, along with the linear fit that was used to determine E_{Gap}. This analysis reveals significant differences in the lineshape of the optical constants corresponding to the interband transitions near 2000 cm^{-1}. In BSTS1, cooling the sample from 300K to 200K, shifts the linear region in $(\epsilon_2(\omega))^2$ to slightly higher ω. Decreasing the temperature further produces two significant changes; the energy gap is shifted to lower energies, and a second linear region appears in $(\epsilon_2(\omega))^2$, indicating a the appearance of a second interband transition, which persists down to 10K. The energy gap is plotted as a function of temperature in Fig. 2c as the black squares, with the second interband transition energy also indicated by the black circles. In contrast, there is only a single linear region in the $(\epsilon_2(\omega))^2$ spectra of BSTS2, which monotonically increases in energy with decreasing temperature. Accordingly, the extracted value of E_{Gap}, plotted in Fig. 2c as the red squares, shifts from 2050 cm^{-1} (0.27 eV) at 300K to the relatively large value 2800 cm^{-1} (0.35 eV) at 10K. One possible explanation for the two transitions identified in BSTS1 is that they originate from slightly different regions in the band structure. At high temperatures, the band structure may be slightly smeared out making the two transitions indistinguishable. With cooling, the possible sharpening of the band structure could reveal the two distinct interband transitions we observe. Unfortunately, there are no temperature dependent measurements of the band structure that could confirm this speculation. An alternative possibility is that we are probing two regions of distinct stoichiometry with our infrared light.

An additional interesting feature is the step-like region in the optical conductivity of BSTS2, detailed in Fig. 3a. These features are reminiscent of the theoretically derived lineshape for the optical constants arising from regions in the band structure where the conduction band ($E_C(\vec{k})$) and valence band ($E_V(\vec{k})$) are parallel [36]. The parallel bands produce a BSCP, where there is a divergence in the joint density of states, resulting in a unique dielectric constant lineshape in the optical response [36, 37].To identify possible locations of these BSCP transitions, we examined the calculated band structure of the related compound, Bi_2Se_3, which was taken from Ref. [7] and plotted in Fig. 3d . From this band structure, we identified four different possible BSCP transitions, which are indicated by the arrows in Fig. 3d. Two of the transitions have almost identical energies, and are therefore likely to manifest as a single BSCP transition. Accordingly both of these transitions have been labeled as CP1 in the schematic, with the remaining two are labeled CP2 and CP3. The BSCP that produce the step-like features in the $\sigma_1(\omega)$ spectra, are indicated in Fig. 3a. The solid lines in Fig. 3e indicate the theoretical energies of the various BSCP transitions. To characterize the measured optical conductivity in terms of BSCP, $\hat{\epsilon} = \epsilon_1 + i\epsilon_2$ was fit using the standard lineshape for a 3-dimensional BSCP [37]:

$$\frac{d^2(\epsilon_1 + i\epsilon_2)}{d\omega^2} = \frac{1}{4} A e^{i\phi} (\omega - \omega_0 + i\xi)^{-3/2}. \qquad (2)$$

The fitting parameters of this equation are: the amplitude (A) which is related to the reduced mass of the two bands, the energy difference between the bands at the BSCP (ω_0) and broadening (ξ), which corresponds to the quasiparticle lifetime [38], and lastly, the phase (ϕ), a value that is related to the band structure in the region near the critical point. The experimentally obtained $d^2\epsilon_1/d\omega^2$ and $d^2\epsilon_2/d\omega^2$are plotted in Fig. 3b and 3c, respectively, along with the best fit lineshape (gray) which consisted of three BSCP. Moreover, the BSCP that produced the resonances in the $d^2\hat{epsilon}/d\omega^2$ spectra are indicated in Fig. 3b and 3c. The parameter ω_0, which was extracted from the fitting of the BSTS2 data, is plotted as a function of temperature in Fig. 3e alongside the transition energies determined from the calculated band structure. Comparing the theoretical values of ω_0 to those extracted from the experimental data reveals that the theoretical energies of CP1 and CP2 differ significantly from the measured values. In contrast, the expected energy of CP3 differed by less than 0.03 eV from the experimental values. These results may indicate that band structure of this system is well understood at energies greater than the energy gap, but is strongly modified from theoretical calculations at lower energies. Currently, no band structure calculations on the $Bi_{2-x}Sb_xTe_{3-y}Se_y$ alloys have been published, but these critical points may serve as useful constraints for future work.

Observation of BSCP requires two ingredients: conservation of momentum ($\vec{k}$), which typically implies a structurally ordered material, and a location in the band structure where a band below E_F is parallel to a band above E_F. The lack of BSCP in BSTS1 indicates that this compound is missing one of the above elements. Our infrared measurements reveal significant differences in the optical response of these two systems, especially near E_{Gap}. The modification to the band structure as the Bi:Sb and Se:Te ratios change may then eliminate the critical points in the band structure. Unfortunately, since photoemission measurements only probe below E_F, experimentally measuring changes to the conduction band with alloying, that could eliminate the CP are very difficult [39]. The crystallographic order, however, has been measured via x-ray diffraction in [28], which demonstrated that the characteristic (1,0,7) and (0,0,12) peaks, indicative of ordering in the chalcogen layers, are present for both BSTS1 and BSTS2. Therefore, the lack of CP in BSTS1 is likely due to the inherent band structure, rather than a reduced crystallographic order.

Although our findings and complimentary photoemission measurements of identically grown samples suggest μ_F resides within the bulk energy gap [39], transport measurements have indicated the presence of an impurity band, in addition to the SS and a surface accumulation

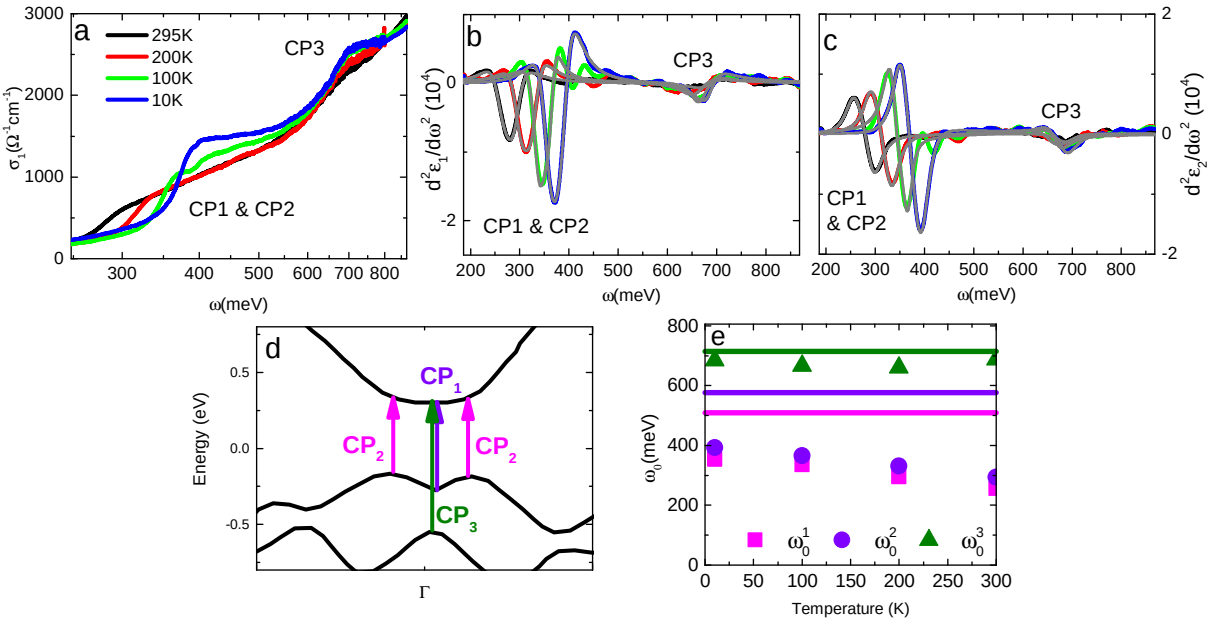

FIG. 3. (a) The step like features in the optical conductivity of BSTS2. The theoretical band structure of Bi_2Se_3 in (d) contains four possible critical points with three different energies that could generate the step like behavior of $\sigma_1(\omega)$. The $d^2\epsilon_1/d\omega^2$ and $d^2\epsilon_2/d\omega^2$ spectra of BSTS2 are plotted in (b) and (c), respectively. The colored lines are the experimental data, and the gray lines are fits to the critical point lineshape (Eq. 4). The critical points corresponding to the step like features in the $\sigma_1(\omega)$ spectra, and the resonances in the $d^2\hat{\epsilon}/d\omega^2$ are indicated in a,b, and c. The energy of the critical points determined from band structure calculations are indicated by horizontal lines, colored to match their respective transition in (d).

layer, that could contribute free carriers to bulk conduction [24]. To quantify the possible role of bulk carriers in these samples, it is useful to independently quantify the free carrier concentration (n). While infrared data cannot precisely measure the value of n, we can estimate n based on the R(ω) spectra at low ω, using the procedure described in the appendix. Our analysis shows that the largest carrier concentration that could be present in this system, yet still be consistent with our experimental reflectance is 4.4×10^{17} cm^{-3}. This value, despite being an upper estimate, places this system among the most insulating TI crystals that have been measured so far [25, 35]. Furthermore, this estimate is based solely on reflectance data and is not anchored by the DC conductivity values measured in [28], which, if included, would reduce this estimate even further.

The CP and spectral analysis discussed above is indicative of a few important aspects of the $Bi_{2-x}Sb_xTe_{3-y}Se_y$ system. First, our measured optical constants show that these alloys are insulators, with a band structure that is strongly modified with cooling. For instance, in BSTS1, a second interband transition is revealed at lower temperatures that is 50% larger in energy than lowest energy transition, E_{Gap}. In BSTS2, E_{Gap} is 0.274 eV at room temperature, but increases by 35% to 0.35 eV with cooling, becoming significantly larger than the 0.3 eV value that is often quoted for pure Bi_2Se_3 [13]. Second, the BSTS2 system confirmed to be a structurally ordered material, as CPs are only observed in systems where $\vec{k}$ is a good quantum number [37, 38]. Since conventional alloying wipes out critical points, the observation of sharply defined CPs in Figs. 3b and 3c are quite remarkable and suggest non-trivial ordering in the BSTS2 alloy. Third, the observation of critical points in BSTS2, which are consistent with transitions at the Γ point, firmly establishes that μ_F is in the bulk energy gap, since any doping into the conduction band would result in occupied states near the Γ point, making them unavailable to transitions from the valence band. Lastly, the upper limits we establish on n place this system among the most insulating TI crystals reported, thereby confirming the effectiveness of alloying in reducing the carrier concentration. The picture that emerges from these findings is that these crystals possess some of the key ingredients thought necessary for observation of surface states, including crystallographic ordering, large energy gap, and low carrier density. Therefore, we tested for the presence of surface states in these materials using magneto optical techniques, which have been demonstrated to be effective tools for the measurement of SS [1, 40, 41].

Magneto-optical spectroscopy is an experimental technique that utilizes the fact that electrons undergo cyclotron motion in the presence of crossed electric and magnetic fields at a characteristic frequency $\omega_c = eB/m^*$ [42]. Importantly, the cyclotron motion results in the splitting of the energy bands into discrete Landau levels

(LL), which are distinguished by their index, l. These LL disperse with field depending on the effective mass of the charge carriers [42–44]. Using infrared spectroscopy, it is possible to excite transitions between LL under the constraint that $|\Delta l| = 1$, yielding absorption features in optical spectra. To compare our magneto optical response, to that expected for LL arising from SS, we calculated the expected LL dispersion using the theoretical framework in [1, 44], and the SS bands described in [24].

In the case of BSTS1, E_F resides at the Dirac point [39], thereby allowing inter-LL transitions, *i.e.* transitions from l_{-n} to l_{n+1}, as illustrated in Fig. 4a. Accordingly we measured the reflectance spectra of both BSTS1 and BSTS2 in the range from 10 meV to 80 meV, where these transitions are expected. The resulting zero-field normalized $(R(H)/R(H = 0T))$ spectra, are shown in Fig. 4b and 4c, for BSTS1 and BSTS2, respectively. There is a noticeable modification to the reflectence with increasing field near 200 cm^{-1}, corresponding to a dip in reflectance arising from the phonon. At higher energies there is some additional noise with increasing H, but overall the spectra are unaffected by the magnetic field. In previous measurements of $Bi_{1-x}Sb_x$, the LL transitions produced changes in the $R(H)/R(H = 0T)$ spectra on the order of 0.01, at fields as small as 3T [43]. Furthermore, these transitions were found to be much more evident in the dR/dH spectra. To illustrate the expected behavior of the magneto-optic features associated with the LL, the calculated energy of the $0 \rightarrow 1$, $-1 \rightarrow 2$ and $-2 \rightarrow 3$ inter-LL transitions are indicated in Fig. 4b and 4c at each field by the gray squares, circles and triangles, respectively. However, these data reveal no anomaly at the expected inter-LL transition energy, nor any feature that shows the expected field dependent behavior. To confirm this, we performed the same dR/dH analysis used in [43] and found the dR/dH spectra to be effectively featureless, lacking any indication of the LL transitions.

Alternatively, we considered the case of BSTS2, where E_F is positioned well above the Dirac point [39], and many of the inter-LL transitions are blocked. Instead, the so called intra-LL transitions occur between adjacent LLs of the same sign, *e.g.* $l_n \rightarrow l_{n+1}$, as illustrated in Fig. 4d. To test for the signatures of the intra-LL transitions, we extended the magneto-reflectance measurements to lower energies (2.5 meV to 12 meV) where they were expected to be most prominent. These low energy $R(H)/R(H = 0T)$ spectra, are shown in Fig. 4e and 4f, for BSTS1 and BSTS2, respectively. As in the discussion of inter-LL transition, the expected intra-LL transition energy at each field is indicated by the gray diamond. Again, there is no feature in these spectra that is consistent with the expected behavior of LL transitions.

The lack of either intra-LL or inter-LL transitions in our magneto optical measurements was an unexpected finding and deserves some consideration. Prior STM measurements of the LL dispersion in the related TI material, Bi_2Se_3, found LLs form only with positive indices ($l \geq 0$) because the lower LLs merge with the bulk valence band [45]. Therefore, when E_F is small, as in BSTS1, the missing LL would inhibit all transitions except for $0 \rightarrow 1$. Moreover, for this transition to be observeable, the E_F would have to be ideally position near the Dirac point, within the small range between the $l = 0$ and $l = 1$ LL, which is approximately 70 meV, at 8T (see Fig. 4a). Even though photoemission has indicated E_F is at the Dirac point in BSTS1[39], aging effects have been observed in similar samples [24], and E_F may simply vary slightly between crystals, possibly making this inter-LL transition unobservable. However, if E_F was shifted upwards by 70 meV, we would still expect to see intra-LL transitions. Since we see neither intra-LL or inter-LL transitions in either sample, there must be an alternative explanation. Interestingly, the observation of critical points in the BSTS2 crystal suggests that it is structurally ordered in the bulk, with a low scattering rate. This observation, in conjuction with the lack of observeable LL transitions implies that the SS are more strongly disordered than the bulk states, with a correspondingly higher scattering rate $(1/\tau)$, which would result in the suppressesion of LL formation, as we observe. Since there was no in-situ cleaving system available in our magneto-optic setup, our samples were cleaved in ambient conditions, and then placed in vacuum for magneto-optic measurements. Possibly, exposure to the environment for this brief time was enough to degrade the BSTS surfaces and introduce strong disorder into the SS, while the crystal bulk remained unaffected. There is support for the hypothesis that the surface electrons are strongly scattered in transport measurements of identically grown BSTS2 crystals [24]. These measurements revealed the scattering time (τ) of the SS electrons was $4.2 \times 10^{-14}s$, corresponding to $1/\tau \approx 800cm^{-1}$ [46].

Another issue that compounds the difficulty of observing the SS LLs via magneto-optical spectroscopy is the small surface carrier density (n_{2D}) of these materials. In the case of identically grown BSTS2 crystals, n_{2D} was found to be approximately 10^{12} cm^{-2} [24]. Such a small carrier density would also reduce the signature of cyclotron motion in reflectance, even with relatively low scattering rates. Indeed Models of the magneto-optical response, detailed later in the text, show that the cyclotron resonance signature in reflectance would be below our measurable range with scattering rates near 200 cm^{-1}. A further discussion of how the scattering rate affects the reflectance measurement at such low carrier densities is presented in the appendix. Likewise, the appendix also contains an explanation for how the high mobility reported in [24], could coexist with the large scattering rate.

Our comprehensive infrared measurements and corresponding analysis of BSTS1 and BSTS2 have revealed both materials to be highly insulating, with the upper limits on the carrier concentration that are among the lowest measured values in crystalline TIs. In addition, the observation of critical points in BSTS2 identifies this

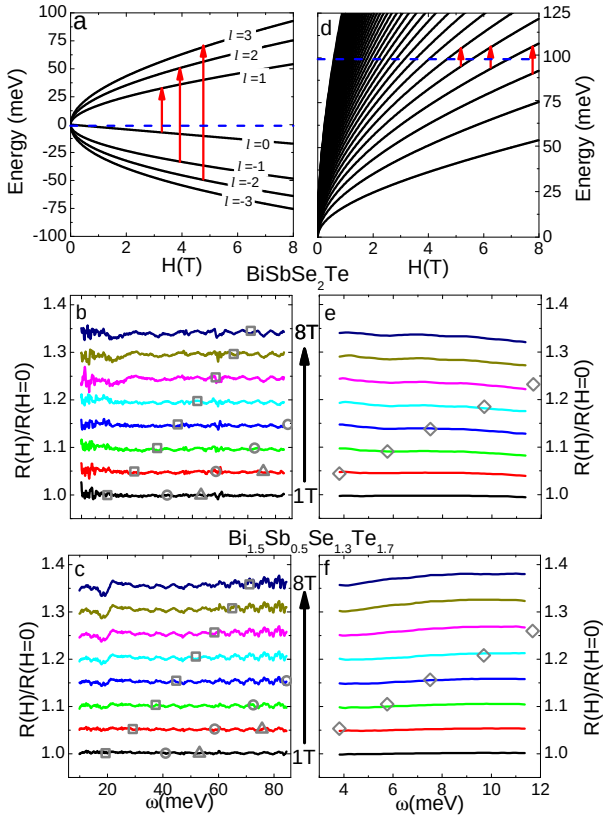

FIG. 4. The LL dispersion of the SS is plotted in (a) along with the allowed transitions (red arrows) assuming E_F (dashed blue line) is at the Dirac point. The field normalized reflectance ($R(H)/R(H=0)$), with increasing fields offset by 0.05, is plotted in (b) and (c) for BSTS1 and BSTS2, respectively. The gray squares, circles and triangles on the experimental (colored) data indicate the expected position of inter-LL transitions, based on the disperion shown in (a). In (d) we schematically show the intra-LL transitions when E_F is well above the Dirac point, with the red arrows indicating transitions between adjacent LL. The low energy $R(H)/R(0)$ spectra for BSTS1 and BSTS2, is shown in (e) and (f), respectively, offset by 0.05. The energy of the intra-LL transitions were calculated assuming $E_F = 100$ meV, and are indicated by the gray diamonds on the experimental data.

alloyed material as crystallographically ordered, which may yield high mobility in the SSs, if the current unknown issues hindering the SSs in $Bi_{2-x}Sb_xTe_{3-y}Se_y$ are resolved. Together, these results indicate that BSTS1 and especially BSTS2 are promising candidates for surface dominated electronic response. However, no signs of SSs were observed in magneto optical measurements, suggesting that μ_F is positioned above the Dirac point, or that the transitions are suppressed by a high scattering rate. Importantly, many of the exotic properties predicted to emerge in TI systems require that μ_F be precisely at the Dirac point, thereby allowing a gap can to be opened in the SSs with a magnetic field [21–23, 47]. Furthermore, it is likely that these phenomena would require high crystallographic order and a low scattering rate for SS electrons. The capability to simultaneously probe each of these elements via IR spectroscopy makes this technique indispensible for identification of ideal TI materials.

This work was partially supported by DOE-BES (DE-FG03-00ER45799), UCOP and JSPS (KAKENHI 25220708), MEXT (Innovative Area "Topological Quantum Phenomena" KAKENHI 22103004), and AFOSR (AOARD 124038). YSL was supported by NRF-2013R1A2A2A01068567.

I. APPENDIX

A. Raw reflectance data

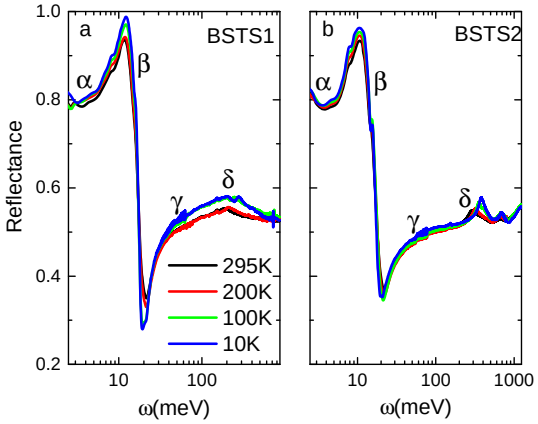

FIG. 5. The raw reflectance is shown for BSTS1 and BSTS2 in panel (a) and (b), respectively. The regions α, β, γ, and δ, that were noted in conductivity, are also indicated here.

The raw reflectance data of BSTS1 and BSTS2 is shown in Fig. 5a and 5b, respectively. Like conductivity, the reflectance spectra exhibit four main regions of interest, with their corresponding label indicated in parenthesis: the low ω region (α), the phonon peak-dip (β), the intragap region (γ) and the interband absorption region (δ). In region α, the reflectivity levels at R=0.76 (0.78) for BSTS1 (BSTS2) at 300K. When cooling to 10K, there is a slight upturn in the reflectivity of BSTS1, and it approaches 0.82 at the lowest accessible frequencies, whereas in BSTS2, reflectivity remains nearly constant with cooling at a level of 0.82. Our observation of $R(\omega) < 1$ at the lowest measured frequencies identifies these materials as non-metallic.

In both samples, we observe a peak dip structure in the β region of reflectivity, indicative of a strong phonon. The peak-dip structure sharpens as temperature is reduced, revealing two slight shoulder features at 68 cm^{-1} and 124 cm^{-1} (63 cm^{-1} and 117 cm^{-1}) in BSTS1 (BSTS2). The phonon structure we observe has

been seen in other TI materials [32–34]. In the intra-gap region γ of BSTS1, we observe an increasing slope as the temperature is lowered from 200K to 100K. The intergap region δ is identified by the peak in conductivity near 2,000 cm^{-1}, which sharpens and blue shifts with decreasing temperature.

In BSTS2, the reflectivity in the intra-gap region γ, remained flat and featureless with decreasing temperature, typical of an insulating material. The higher energy region δ, can be clearly identified as the peak in reflectivity, corresponding to the onset of interband absorption, which sharpens and blue shifts with decreasing temperature. A second peak in reflectivity is noticeable at 5000 cm^{-1} indicating a second interband transition. This peak, in contrast to the lower energy feature, does not shift noticeably with temperature.

B. Carrier density upper limit

In the presence of free carriers, R(ω) will approach 1 as $\omega \to 0$, corresponding to the so called Drude peak in optical conductivity. Conversely, in the absence of free carriers, R(ω)will remain constant at a value smaller than 1 (see Fig. 5). It is important to note that within our experimental range of, there is no evidence to suggest that R(ω) approaches 1. However, we have considered the scenario that there are free carriers in these materials, but the characteristic increase in R(ω) towards 1 simply occurs below our experimental range. Accordingly, we show the experimental reflectance at 10K for BSTS1 and BSTS2, in Fig. 6a and 6b, along with two alternative low extrapolations. The corresponding values of $\sigma_1(\omega)$, obtained from the extrapolated R(ω) spectra via KK inversion, are plotted Fig. 6c and 6d. As expected, the low frequency extrapolation to 1 results in a finite value of $\sigma_1(\omega)$ as $\omega \to 0$, producing a weak Drude peak. On the other hand the flat extrapolation results in $\sigma_1(\omega)$ spectra that approaches 0 at low ω. We modeled the extracted spectra of $\sigma_1(\omega)$ with a single Drude oscillator and a Lorentz oscillator to capture the phonon peak. These fits are indicated in Fig. 6c and 6d by the dashed gray lines on top of the experimental data. Since the Drude oscillator strength (ω_p^2) is directly related to the carrier density (n) via [46]:

$$\omega_p^2 = \frac{ne^2}{\epsilon_0 m^*}, \tag{3}$$

the carrier density arising from the Drude peak could be extracted assuming an effective mass of $0.11m_e$ as measured in Bi_2Te_2Se [35]. The resulting maximum carrier concentrations (n_0^{max}), indicated in Fig. 6c and 6d, are $1.57 \times 10^{17} cm^{-3}$ and $4.36 \times 10^{17} cm^{-3}$ for BSTS1 and BSTS2, respectively. These values, despite being upper limits, are among the lowest values of n reported for TI crystals [25, 35, 48]. Additionally, the maximum Fermi energy (E_F^{max}), within the bulk conduction band, could be extracted from the carrier density, assuming parabolic bands [49]. The resulting values of E_F^{max} are 9 meV (19 meV) for BSTS1 (BSTS2). Using these values of E_F^{max}, it was possible to also estimate the maximum surface carrier density (n_{2D}^{max}) in these crystals. To make this estimations we assumed that the valence band edge is at the Dirac point, as indicated by photoemission measurements [39]. Then, the Fermi energy of the SS (E_F^{ss}), relative to the Dirac point, would be given simply by $E_F^{max} + E_g$, as illustrated in Fig. 6e and 6f. Once E_F^{ss} is determined, n_{2D}^{max} is then simply given by [50]:

$$n_{2D}^{max} = \left(\frac{E_F}{\hbar v_0}\right)^2 \frac{1}{4\pi}. \tag{4}$$

The resulting values of n_{2D}^{max} are $7.7 \times 10^{11} cm^{-2}$ ($3.9 \times 10^{12} cm^{-2}$) for BSTS1 (BSTS2). The intra-LL dispersions, associated with these Fermi energies, are plotted in Fig. 6g. These energy dispersion curves lie within our measurable range, as shown in Fig. 4, yet were unobservable. Importantly, the values of n_{2D}^{max} should only be considered as upper limits, rather than definite estimates. Likewise, the scattering rate associated with these values of n_{2D}, 33 cm^{-1} (41 cm^{-1}) in BSTS1 (BSTS2) should be considered lower limits. Indeed, the intra-LL dispersion associated with these values of n_{2D}^{max} should be observable with such low scattering rates. Instead, the overall lack of measurable LL features suggests the SS have a much higher scattering rate, with a correspondingly smaller carrier density.

C. Mobility and scattering rate

The relatively high mobility of $9.8{\times}10^2$ $cm^2/(V{\cdot}s)$ reported for BSTS1 seems to conflict with the large scattering rate of 800 cm^{-1} [24]. However, this can be understood by considering the relationship between mobility (μ), carrier density (n) and scattering rate (τ) in Dirac electron systems [51]:

$$\mu = \frac{e\tau v_F}{2\hbar\sqrt{\pi n}} \tag{5}$$

While μ is directly proportional to the scattering time, it is also inversely proportional to the carrier density. Thus, a low carrier density will overcome the small scattering time to yield a relatively high mobility. To illustrate the effects of a large scattering rate on our experimental data, we have modeled the reflectance spectra using a 2D surface carrier density of 10^{12} cm^{-2}, as was found in similarly grown crystals, with various scattering rates. To illustrate the changes that would be expected assuming different scattering rates, the modeled reflectance ratios R(H=8T,Γ)/ R(H=0T,Γ) shown in Fig. 7. There is a noticeable modification to the reflectance spectra when Γ=20 cm^{-1}, but when Γ approaches more reasonable values of 200 cm^{-1}, the signature becomes much weaker, and is likely undetectable, based on signal to noise limitations.

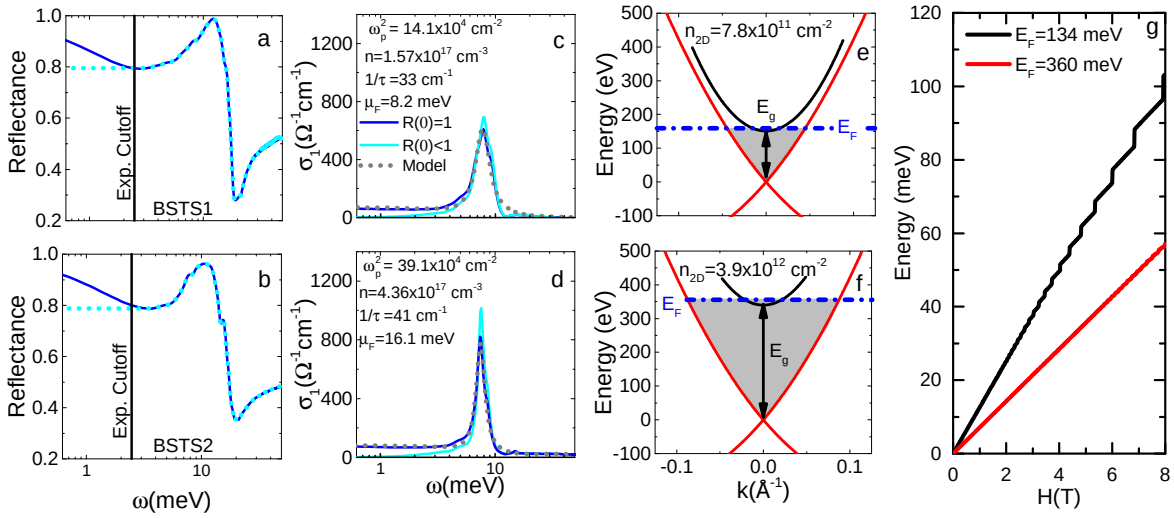

FIG. 6. The measured reflectance of BSTS1 (a) and BSTS2 (b) are shown with the low two types of low frequency extrapolations. The solid blue line assumes reflectance goes to 1 at low frequencies, as is typical for metals, whereas the dashed cyan line assumes a flat reflectance, as expected for an insulator. The $\sigma_1(\omega)$ extracted via KK inversion for either type of extrapolation is shown in (c) and (d) for BSTS1 and BSTS2, colored to match the reflectance data. A simple Drude-Lorentz fit to $\sigma_1(\omega)$ is also plotted as the dashed gray line. The Drude oscillator strength (ω_p^2) obtained from this fit, and indicated in (c) and (d), was used to determine the maximum bulk carrier density (n_0^{max}) in each system. Likewise, the scattering rate associated with this Drude oscillator is also indicated. The maximum value of the Fermi energy in the bulk conduction bands (E_F^{max}) was then determined from n_0. And is indicated in (e) and (f) for BSTS1 and BSTS2, respectively. The two dimensional surface carrier density (n_{2D}) corresponding to E_F^{max} in both systems was then determined and is also shown in (e) and (f). The expected field dispersion of the intra-LL transitions, corresponding to the carrier densities obtained in (e) and (f) are plotted in (g).

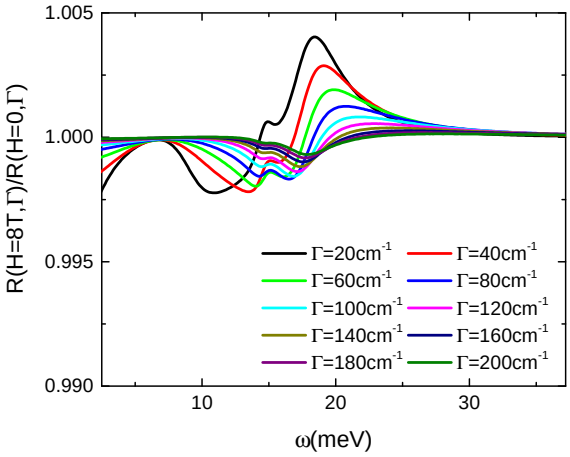

FIG. 7. The modeled reflectance ratios of BSTS2 are plotted at H=8T, assuming a 2D carrier density of 10^{12} cm^{-2} and different scattering rates (Γ). As Γ increases from 20cm^{-1} to 200 cm^{-1} , the modification to the reflectance spectra is reduced from 0.4% to below 0.05%.

[1] A. Schafgans, K. W. Post, a. a. Taskin, Y. Ando, X.-L. Qi, B. C. Chapler, and D. N. Basov, Physical Review B **85**, 195440 (2012).

[2] B. A. Bernevig and S.-C. Zhang, Physical Review Letters **96**, 106802 (2006).

[3] B. A. Bernevig, T. L. Hughes, and S.-C. Zhang, Science (New York, N.Y.) **314**, 1757 (2006).

[4] L. Fu, C. Kane, and E. Mele, Physical Review Letters **98**, 106803 (2007).

[5] C. L. Kane and E. J. Mele, Physical Review Letters **95**, 226801 (2005).

[6] C. Kane and E. Mele, Physical review letters **146802**, 1 (2005).

[7] H. Zhang, C.-X. Liu, X.-L. Qi, X. Dai, Z. Fang, and S.-C. Zhang, Nature Physics **5**, 438 (2009).

[8] D. Hsieh, D. Qian, L. Wray, Y. Xia, Y. S. Hor, R. J. Cava, and M. Z. Hasan, Nature **452**, 970 (2008).

[9] A. Taskin and Y. Ando, Physical Review B **80**, 085303 (2009).

[10] A. Nishide, A. a. Taskin, Y. Takeichi, T. Okuda, A. Kakizaki, T. Hirahara, K. Nakatsuji, F. Komori, Y. Ando, and I. Matsuda, Physical Review B **81**, 041309 (2010).

[11] D. Hsieh, Y. Xia, L. Wray, D. Qian, a. Pal, J. H. Dil, J. Osterwalder, F. Meier, G. Bihlmayer, C. L. Kane, Y. S. Hor, R. J. Cava, and M. Z. Hasan, Science (New York, N.Y.) **323**, 919 (2009).

[12] M. König, S. Wiedmann, C. Brüne, A. Roth, H. Buhmann, L. W. Molenkamp, X.-L. Qi, and S.-C. Zhang, Science (New York, N.Y.) **318**, 766 (2007).

[13] Y. Xia, D. Qian, D. Hsieh, L. Wray, a. Pal, H. Lin, a. Bansil, D. Grauer, Y. S. Hor, R. J. Cava, and M. Z. Hasan, Nature Physics **5**, 398 (2009).

[14] Y. Ando, Journal of the Physical Society of Japan **82**, 1 (2013).

[15] M. Z. Hasan and C. L. Kane, Reviews of Modern Physics **82**, 3045 (2010).

[16] X. L. Qi and S. C. Zhang, Reviews of Modern Physics **83** (2011), 10.1103/RevModPhys.83.1057, arXiv:1008.2026.

[17] M. Z. Hasan and J. E. Moore, Annual Review of Condensed Matter Physics **2**, 55 (2010), arXiv:1011.5462.

[18] A. Essin, J. Moore, and D. Vanderbilt, Physical Review Letters **102**, 146805 (2009).

[19] J. E. Moore, Nature **464**, 194 (2010).

[20] X.-L. Qi, T. L. Hughes, and S.-C. Zhang, Phys. Rev. B **78**, 195424 (2008).

[21] J. Maciejko, X.-L. Qi, H. D. Drew, and S.-C. Zhang, Phys. Rev. Lett. **105**, 166803 (2010).

[22] W.-K. Tse and A. H. MacDonald, Phys. Rev. Lett. **105**, 57401 (2010).

[23] W.-K. Tse and a. H. MacDonald, Physical Review B **84**, 205327 (2011).

[24] a. a. Taskin, Z. Ren, S. Sasaki, K. Segawa, and Y. Ando, Physical Review Letters **107**, 016801 (2011).

[25] D. Kim, S. Cho, N. P. Butch, P. Syers, K. Kirshenbaum, S. Adam, J. Paglione, and M. S. Fuhrer, Nature Physics **8**, 460 (2012).

[26] L. He, F. Xiu, X. Yu, M. Teague, W. Jiang, Y. Fan, X. Kou, M. Lang, Y. Wang, G. Huang, N.-C. Yeh, and K. L. Wang, Nano letters **12**, 1486 (2012).

[27] J. Horak, Z. Stary, P. Lostak, and J. Pancir, **51**, 1353 (1990).

[28] Z. Ren, A. a. Taskin, S. Sasaki, K. Segawa, and Y. Ando, Physical Review B **84**, 165311 (2011).

[29] M. Neupane, S.-Y. Xu, L. a. Wray, a. Petersen, R. Shankar, N. Alidoust, C. Liu, a. Fedorov, H. Ji, J. M. Allred, Y. S. Hor, T.-R. Chang, H.-T. Jeng, H. Lin, a. Bansil, R. J. Cava, and M. Z. Hasan, Physical Review B **85**, 235406 (2012).

[30] S. Jia, H. Beidenkopf, I. Drozdov, M. K. Fuccillo, J. Seo, J. Xiong, N. P. Ong, A. Yazdani, and R. J. Cava, Phys. Rev. B **86**, 1 (2012).

[31] M. Dressel and G. Gruener, *American Journal of Physics*, 1st ed., Vol. 70 (Cambridge University Press, New York, New York, USA, 2002).

[32] P. Di Pietro, F. M. F. Vitucci, D. Nicoletti, L. Baldassarre, P. Calvani, R. Cava, Y. S. Hor, U. Schade, S. Lupi, and P. D. Pietro, Physical Review B **86**, 1 (2012), arXiv:arXiv:1201.5609v1.

[33] a. D. LaForge, a. Frenzel, B. C. Pursley, T. Lin, X. Liu, J. Shi, and D. N. Basov, Physical Review B **81**, 125120 (2010).

[34] A. a. Reijnders, Y. Tian, L. J. Sandilands, G. Pohl, I. D. Kivlichan, S. Y. F. Zhao, S. Jia, M. E. Charles, R. J. Cava, N. Alidoust, S. Xu, M. Neupane, M. Z. Hasan, X. Wang, S. W. Cheong, and K. S. Burch, Physical Review B **89**, 075138 (2014).

[35] Z. Ren, A. A. Taskin, S. Sasaki, K. Segawa, and Y. Ando, Phys. Rev. B **82**, 1 (2010).

[36] M. Yu, Peter Y., Cardona, *Fundamentals of Semiconductors. Graduate Texts ...* (2010).

[37] P. Lautenschlager and M. Garriga, Physical Review B **35**, 9174 (1987).

[38] K. Burch, J. Stephens, R. Kawakami, D. Awschalom, and D. Basov, Physical Review B **70**, 205208 (2004).

[39] T. Arakane, T. Sato, S. Souma, K. Kosaka, K. Nakayama, M. Komatsu, T. Takahashi, Z. Ren, K. Segawa, and Y. Ando, Nature communications **3**, 636 (2012).

[40] G. S. Jenkins, a. B. Sushkov, D. C. Schmadel, N. P. Butch, P. Syers, J. Paglione, and H. D. Drew, Physical Review B **82**, 125120 (2010).

[41] R. Valdés Aguilar, a. V. Stier, W. Liu, L. S. Bilbro, D. K. George, N. Bansal, L. Wu, J. Cerne, a. G. Markelz, S. Oh, and N. P. Armitage, Physical Review Letters **108**, 087403 (2012).

[42] E. Palik and J. Furdyna, Reports on Progress in Physics **1193** (1970).

[43] a. a. Schafgans, S. J. Moon, B. C. Pursley, a. D. LaForge, M. M. Qazilbash, a. S. Sefat, D. Mandrus, K. Haule, G. Kotliar, and D. N. Basov, Physical Review Letters **108**, 147002 (2012).

[44] C.-X. C. Liu, X.-L. X. Qi, H. H. Zhang, X. Dai, Z. Fang, and S.-C. Zhang, Physical Review B **82**, 045122 (2010).

[45] P. Cheng, C. Song, T. Zhang, Y. Zhang, Y. Wang, J.-F. Jia, J. Wang, Y. Wang, B.-F. Zhu, X. Chen, X. Ma, K. He, L. Wang, X. Dai, Z. Fang, X. Xie, X.-L. Qi, C.-X. Liu, S.-C. Zhang, and Q.-K. Xue, Physical Review Letters **105**, 076801 (2010).

[46] D. C. Johnston, Advances in Physics **59**, 803 (2010), arXiv:1005.4392.

[47] X. Qi, R. Li, J. Zang, and S. Zhang, Science **323**, 1184 (2009).

[48] N. P. Butch, K. Kirshenbaum, P. Syers, a. B. Sushkov, G. S. Jenkins, H. D. Drew, and J. Paglione, Physical Review B **81**, 241301 (2010).

[49] C. Kittel, *Introduction to Solid State Physics*, 8th ed. (2005).

[50] D. N. Basov, M. M. Fogler, a. Lanzara, F. Wang, and Y. Zhang, Reviews of Modern Physics **86**, 959 (2014), arXiv:1407.6721.

[51] a. H. Castro Neto, N. M. R. Peres, K. S. Novoselov, and a. K. Geim, Reviews of Modern Physics **81**, 109 (2009).